Editors' Suggestion

Magnetostriction-Driven Muon Localization in an Antiferromagnetic Oxide

Pietro Bonfà,[1,*] Ifeanyi John Onuorah,[1] Franz Lang,[2] Iurii Timrov,[3] Lorenzo Monacelli,[3] Chennan Wang,[4] Xiao Sun,[5,†] Oleg Petracic,[5] Giovanni Pizzi,[6] Nicola Marzari,[3,6] Stephen J. Blundell,[7] and Roberto De Renzi[1]

[1]*Dipartimento di Scienze Matematiche, Fisiche e Informatiche, Universitá di Parma, I-43124 Parma, Italy*
[2]*ISIS Neutron and Muon Source, STFC Rutherford Appleton Laboratory, Chilton, Didcot OX11 0QX, United Kingdom*
[3]*Theory and Simulation of Materials (THEOS), and National Centre for Computational Design and Discovery of Novel Materials (MARVEL), École Polytechnique Fédérale de Lausanne, 1015 Lausanne, Switzerland*
[4]*Laboratory for Muon Spin Spectroscopy, Paul Scherrer Institute, CH-5232 Villigen, Switzerland*
[5]*Jülich Centre for Neutron Science JCNS-2 and Peter Grünberg Institute PGI-4, JARA-FIT, Forschungszentrum Jülich GmbH, 52425 Jülich, Germany*
[6]*Laboratory for Materials Simulations (LMS), Paul Scherrer Institut (PSI), CH-5232 Villigen PSI, Switzerland*
[7]*Department of Physics, University of Oxford, Clarendon Laboratory, Oxford OX1 3PU, United Kingdom*

(Received 2 June 2023; revised 18 September 2023; accepted 20 November 2023; published 24 January 2024)

Magnetostriction results from the coupling between magnetic and elastic degrees of freedom. Though it is associated with a relatively small energy, we show that it plays an important role in determining the site of an implanted muon, so that the energetically favorable site can switch on crossing a magnetic phase transition. This surprising effect is demonstrated in the cubic rocksalt antiferromagnet MnO which undergoes a magnetostriction-driven rhombohedral distortion at the Néel temperature $T_N = 118$ K. Above T_N, the muon becomes delocalized around a network of equivalent sites, but below T_N the distortion lifts the degeneracy between these equivalent sites. Our first-principles simulations based on Hubbard-corrected density-functional theory and molecular dynamics are consistent with the experimental data and help to resolve a long-standing puzzle regarding muon data on MnO, as well as having wider applicability to other magnetic oxides.

DOI: 10.1103/PhysRevLett.132.046701

The coupling between the magnetization and the lattice can result in a deformation, called magnetostriction. This magnetostructural interaction is rather weak and, for example, in insulating magnets containing transition-metal ions, is dwarfed by the much larger magnetic superexchange interaction between localized magnetic moments. A commonly used technique to study such magnetic materials is muon-spin spectroscopy (μSR) [1], in which a spin-polarized positive muon is implanted in a sample primarily under the effect of electrostatic forces (therefore preserving its spin polarization while losing kinetic energy). For this reason, it has not been expected that the much smaller magnetostructural couplings should play any role in determining the experimental signal. In this Letter, we demonstrate the surprising fact that, below a magnetic phase transition, exchange-driven effects can drastically change the nature of the muon state, so that the muon switches its energetically favorable position as the sample is cooled through the Néel temperature T_N. Our study is focused on the prototypical antiferromagnet manganese oxide (MnO), but we describe an approach that has wider applicability in other magnetic oxides.

Magnetic order in MnO was identified over 65 years ago [2] and later progressively refined with numerous studies [3–10]. For temperatures above $T_N = 118$ K, MnO has the cubic rocksalt structure ($Fm\bar{3}m$). Below T_N a magnetic transition to antiferromagnetic (AFM) ordering (type-II) occurs, with Mn moments aligned ferromagnetically along (111) planes (likely along the $[11\bar{2}]$ direction [5]), and antiparallel between adjacent planes, which induces a small distortion. This magnetostrictive effect, associated with a deviation of ∼0.6° from the 90° angle in the cubic structure [11,12], results in a rhombohedral distortion that is further refined by neutron scattering experiments into the monoclinic $C2/c$ symmetry of the magnetically ordered phase. An additional modulation of the atomic positions further reducing the symmetry to $C2$ has also been suggested [5].

Previous experiments on MnO using μSR [1] show that (i) in zero applied field (ZF) a single precession frequency is observed for all $T < T_N$ [13,14], which up to now has been interpreted to imply a highly symmetric muon site, identified as the $(\frac{1}{4}, \frac{1}{4}, \frac{1}{4})$ interstitial $(8c)$ of the conventional cubic cell, and (ii) transverse field (TF) measurements for $T > T_N$ reveal a large negative Knight shift which is not proportional to the susceptibility [15,16], but shows an unusual *time dependence*, so that the estimate of the Knight shift depends on the time interval used to fit the experimental asymmetry [17]. This latter observation can be rationalized [15] by assuming that the muon exhibits a

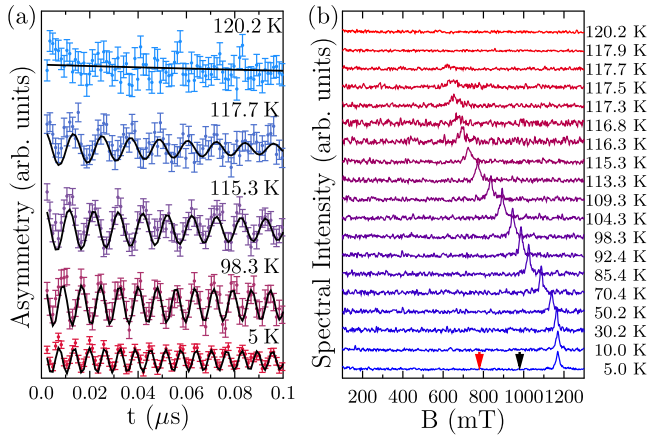

FIG. 1. (a) Muon asymmetry $A(t)$ of single crystal MnO at selected temperatures. The black line is a fit to the function $A(t) = A_b + A_o \cos(\gamma_\mu B_\mu t) \exp(-\lambda t)$, where B_μ is the local field at the muon site, γ_μ is the muon gyromagnetic ratio, and the baseline (A_b) and oscillating (A_o) amplitudes depend on the setup of the experiment. (b) Fourier transform of $A(t)$ at various temperatures. The red and black arrows are the prediction of the local field at the muon site obtained from DFT considering *ab initio* or experimental contact field, respectively, while the dipolar part is computed assuming $4.9\mu_B$ per Mn atom. Data for various temperatures are displaced vertically on both panels for clarity.

thermally activated diffusion between sites and ends up close to a Mn vacancy [18,19], with the analysis of the time dependence of the Knight shift yielding an activation energy for this process of about 800 K [15,20]. An additional transition between 400 and 600 K has been detected in the exponential depolarization rate of the ZF signal [21] and may be related to a change in the orbital occupation of Mn-3d orbitals [22,23], though this interpretation has not been supported by a quantitative prediction. Moreover, the suggested muon site at the interstitial $(\frac{1}{4},\frac{1}{4},\frac{1}{4})$ position would place the muon surprisingly far from the electronegative oxygen atoms, but displacing it from this symmetrical position was assumed to lead to more than one local field at the muon site below T_N, in contrast with experiment. The single precession frequency for $T < T_N$ is confirmed by our new results collected on a single crystal of MnO (characterized in Ref. [24]). The effect is demonstrated both in the raw muon asymmetry [Fig. 1(a)] and in its Fourier transform [Fig. 1(b)]; see the Supplemental Material (SM) [25] for further details.

To interpret the experimental data, we performed density-functional theory (DFT) [26,27] simulations using Hubbard corrections [28,68], in particular using extended Hubbard functionals [29]. The electronic structure of MnO is described using the PBEsol functional [30], while self-interaction errors are alleviated using on-site $U = 4.84$ eV and intersite $V = 0.36$ eV Hubbard parameters for Mn(3d) and Mn(3d) − O(2p), respectively, computed self-consistently using density-functional perturbation theory [31,32]. The additional intersite parameter $V = 0.50$ eV is obtained for Mn(3d) − H(1s) when considering the muon. For *ab initio* molecular dynamics (MD) simulations, used to train machine-learned force fields, and for nudged elastic band simulations (see SM [25]), we used the PZ-LDA functional [33] and an averaged on-site Hubbard $U = 5$ eV.

The rhombohedral distortion of the antiferromagnetic phase [69], predicted by DFT as reported in many previous studies [3,12,70–74], is well reproduced and the PBEsol + $U + V$ unit cell volume of 22.14 Å^3 (21.89 Å^3 within LDA + U) deviates from the experiment only by ∼2%. The addition of a gradient correction in the exchange-correlation term and the intersite contribution in the Hubbard correction alter the position found for the muon by a small margin (< 0.1 Å), slightly alter the contact term (by ∼15%), and enhance embedding site energy differences (by ∼40%).

From an analysis of the muon embedding sites two important points emerge, providing a novel interpretation of the experimental findings: (i) μ^+ does not stop in the $(\frac{1}{4},\frac{1}{4},\frac{1}{4})$ position and the stable locations are instead closer to the oxygen atoms, and (ii) different equilibrium positions are observed in the low-temperature rhombohedrally distorted structure and in the high-temperature cubic lattice (with Wyckoff site symmetries 2c and 6h in the rhombohedral $[R\bar{3}m]$ and 32f in the cubic $[Fm\bar{3}m]$ phases). The equilibrium positions (Table I) for both structures are shown in Fig. 2, and, collectively, they form a cube around each oxygen atom. Two colors are used to distinguish the geometrically inequivalent sites in the rhombohedral cell, while the numbers identify sites with different absolute values of the local field in the AFM phase. In the rhombohedral phase there are only sites of kind 1 (orange spheres) since the higher energy sites (green spheres) are unstable owing to the absence of any barrier separating them from the lowest energy sites (see SM [25]). The direct consequence of this observation is that these interstitial muon sites close to oxygen atoms produce a single precession frequency in the AFM phase, compatible with experimental observations without requiring the μ^+ to stop far away from the O atoms in $(\frac{1}{4},\frac{1}{4},\frac{1}{4})$ and thus solving one of the parts of the puzzle. This frequency can be estimated from $\mathbf{B}_\mu = \mathbf{B}_{\text{dip}} + \mathbf{B}_{\text{cont}}$, which is the sum of the dipolar and Fermi contact contributions. The first term, due to the dipolar interaction of the muon with the distant 3d spin-polarized electrons, is computed assuming (classical) magnetic dipoles $\mathbf{m}$ at the Mn atomic positions. We set $|\mathbf{m}| = 4.9\mu_B$ following the recent experimental estimates [4,75–77] and we consider the displacement due to the presence of the interstitial positive muon [78]. The contact term is instead evaluated from DFT [79] (reported as B_{cont}), or obtained experimentally (see SM [25]).

TABLE I. Results of *ab initio* analysis of muon sites. Energies are in meV relative to the lowest energy site and local fields are in Tesla. Sites are labeled according to Fig. 2 and their position is in crystal coordinates with respect to the $2 \times 2 \times 2$ conventional cubic or rhombohedral supercell where Mn is at the origin. $\mathbf{B}_{\mathrm{dip}}$ is the dipolar field at the muon sites computed in the locally distorted lattice. $\mathbf{B}_{\mathrm{cont}}$ is the contact field obtained from DFT simulations. The last two columns are the absolute values of the dipolar contribution and the total field at the muon site in the AFM phase.

Lattice	Site	Position	$E - E_0$	$\mathbf{B}_{\mathrm{dip}}$	$\mathbf{B}_{\mathrm{cont}}$	$\lvert\mathbf{B}_{\mathrm{dip}}\rvert$	$\lvert\mathbf{B}_{\mathrm{dip}} + \mathbf{B}_{\mathrm{cont}}\rvert$
Rhombohedral	1	(0.19, 0.19, 0.19) (0.31, 0.31, 0.31)	0	(−0.47, −0.47, 0.94) (0.47, 0.47, −0.94)	(0.1, 0.1, −0.2) (−0.1, −0.1, 0.2)	1.13	0.8
Cubic	1	(0.19, 0.19, 0.19) (0.31, 0.31, 0.31)	32	(−0.42, −0.42, 0.84) (0.42, 0.42, −0.84)	(0.1, 0.1, −0.3) (−0.1, −0.1, 0.3)	1.12	0.8
	2	(0.31, 0.19, 0.31) (0.31, 0.19, 0.19) (0.19, 0.31, 0.19) (0.19, 0.31, 0.31)	0	(0.68, −0.30, −0.81) (0.30, −0.68, 0.81) (−0.68, 0.30, 0.81) (−0.30, 0.68, −0.81)	< 0.1	1.13	1.1
	3	(0.31, 0.31, 0.19) (0.19, 0.19, 0.31)	0	(0.13,0.13,0.58) (−0.13, −0.13, −0.58)	< 0.1	0.57	0.6

The estimated local fields at the muon sites are summarized in Table I. The local field at the muon site appears to be slightly underestimated, with a predicted value of $B_\mu = 0.8$ T instead of the 1.17 T observed experimentally for $T \to 0$ K, as shown by the red arrow in Fig. 1(b). Notably, the (negative) contact hyperfine coupling estimated from Hubbard-corrected DFT is slightly larger than the one obtained from TF experiments [16]. This discrepancy is not surprising [34] and the estimate may possibly be improved by taking into account anharmonic effects [35]. The smaller contact field contribution obtained in Ref. [16] improves the experimental agreement, as shown by the black arrow in Fig. 1(b). The additional monoclinic distortion of the structure [5] does not alter this picture, but the further modulation of atomic positions discussed in Ref. [5] would result in a ∼250 mT splitting of the local field at the muon site, much larger than the observed width of 50 mT; however, this proposed modulation was not identified in a recent magnetic pair distribution function study [80].

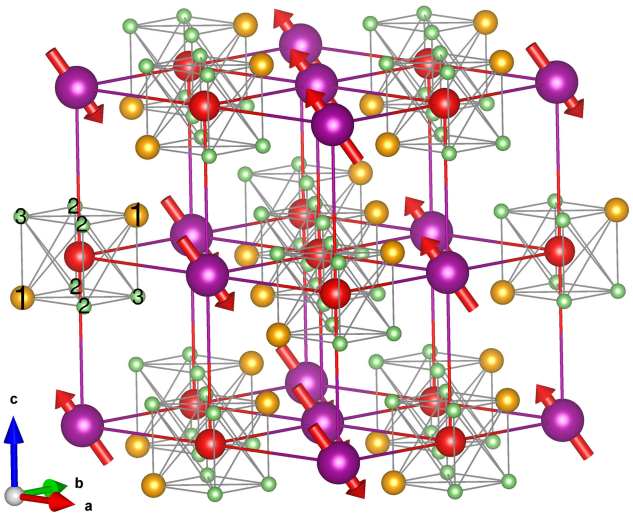

FIG. 2. Muon sites in MnO. The arrows on Mn (purple) spheres show the magnetic order; oxygen is shown as red spheres. The muon sites are shown by orange and green spheres (to distinguish symmetrically inequivalent sites 2*c* and 6*h* in the rhombohedral cell) and labeled 1, 2, and 3 to identify muon sites with the same $|\mathbf{B}_\mu|$ in the AFM phase.

In the high-temperature cubic phases, modeled using the same spin texture but constraining the lattice angles to 90°, the situation is reversed: the lowest energy sites are the ones labeled 2 and 3 in Fig. 2 (the green spheres, sites 1 are 32 meV higher in energy; see Table I and SM [25]). These sites have almost zero hyperfine contact term (estimated from DFT) and different $\mathbf{B}_{\mathrm{dip}}$ contributions. Note that the average local field experienced by a muon hopping between sites 1, or 3, or among sites 2 would vanish. The average field would vanish *a fortiori* when hopping among all three kinds of sites. This clearly does not happen in the rhombohedral structure up to T_{N}, since the internal field is detected up to the transition. The energy difference between geometrically equivalent sites is a direct consequence of the magnetic order that breaks the cubic symmetry and induces a substantial electron-density redistribution [81] observed experimentally [82,83] even in the high-temperature cubic phase [84]. Therefore, contrary to naive expectations, the muon local energy landscape is ultimately dictated by the magnetic exchange interactions, despite the small energy associated with magnetostriction [85]. The effect is highly nontrivial since it manifests itself in a combination of magnetostrictive lattice distortion and charge order. The latter lifts the degeneracy of the eight equivalent muon sites in the cubic crystal, and even makes some of them (the green ones in Fig. 2) unstable in the rhombohedral structure. This assignment reconciles the observed μSR signal with the general expectation that positive muons occupy positions close to electronegative atoms.

Having clarified the description of the ZF results in the magnetically ordered phase, we focus now on the temperature dependence of the ZF depolarization rate and on the Knight shift in the paramagnetic phase. As already mentioned, the peculiar time-dependent behavior of the Knight shift [17,20] and the slow temperature variation of the ZF relaxation rates observed in the range $T_N < T < 300$ K can be interpreted using a diffusion model that assumes single hops to a second "site" with a different Knight shift [15]. In addition, a second jump in the ZF depolarization rate at 540 K was reported [21]. Both effects can be understood in the light of multiple interstitial sites present in the cubic phase around the oxygen atoms, all separated by small energy barriers (see SM [25]). A thermally activated delocalization of the muon on the energy minima around the oxygen forms in the cubic phase: This new state is expected to show zero dipolar contribution to the Knight shift for symmetry reasons. At even higher temperatures the muon will diffuse incoherently throughout the crystal and possibly reach Mn vacancies where a different Knight shift is probed. We therefore expect two distinct dynamic processes, a locally confined dynamics around a single O atom and a second regime of classical hopping among sites coordinated to different O atoms, thereby explaining both experimental observations. A quantitative estimation of the consequent time-dependent Knight shift is hardly possible owing to the large uncertainty in the impurity concentration [86,87] and the parameters of the diffusion process reported below.

An accurate description of the muon states as a function of temperature, which involves also the analysis of the structural transition, is beyond the scope of the present work, since it requires detailed, computationally very intensive estimations of the vibrational contributions to the free energy (from both the lattice and the muon) as a function of temperature. However, qualitative support for the existence of two states may be obtained with molecular dynamics simulations, using machine-learned force fields trained from *ab initio* MD in the cubic symmetry. Classical MD is inappropriate at low temperatures owing to the small mass of the muon (about 1/9 of the proton), but the quantum contribution to the dynamics becomes progressively less relevant at higher temperature.

A 64-atom supercell plus the muon is initialized in the lowest energy configuration, assigned random velocities according to the Maxwell-Boltzmann distribution, thermalized using a Nosé-Hoover thermostat for 50 fs, and eventually evolved with microcanonical dynamics to rule out any possible influence of the thermostat on the dynamics. From the MD trajectories we first compute the angular autocorrelation function $\phi_{\mu\text{-O}}(\tau) = \langle \hat{\mathbf{r}}(t) \cdot \hat{\mathbf{r}}(t+\tau) \rangle$ for the muon bound to an oxygen using

$$\phi_{\mu\text{-O}}(\tau) = \frac{1}{N_s - n_\tau} \sum_{j=1}^{N_s - n_\tau} \hat{\mathbf{r}}_{\mu\text{-O}}(t_j + \tau) \cdot \hat{\mathbf{r}}_{\mu\text{-O}}(t_j), \quad (1)$$

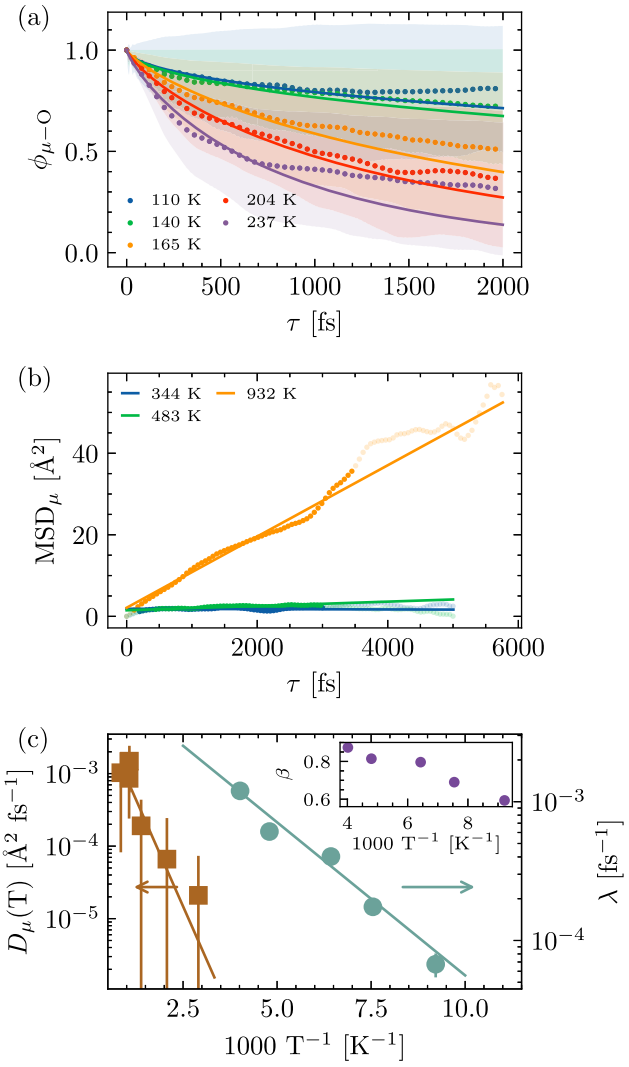

FIG. 3. Results from MD simulations. (a) Angular autocorrelation function, Eq. (1), for a muon bound to an oxygen, with solid fit curves (see text). Shaded areas display the uncertainty. (b) The MSD of the muon. Solid lines are linear fit to the data highlighted by opaque points. (c) Muon diffusion coefficient (brown squares) and decay rate of the angular autocorrelation function (turquoise circles) as a function of the inverse temperature, together with fits to Arrhenius equations (see main text). Finally, the inset shows the values obtained for the exponent of the stretched exponential fits shown in (a).

where $\hat{\mathbf{r}}_{\mu\text{-O}}$ is the unit vector joining the muon and the oxygen atom it binds to, N_s is the total amount of molecular dynamics steps, and $n_\tau = \tau/\Delta t$, where Δt is a time step of the simulation. The maximum n_τ is set to $N_s/2$ in Eq. (1) in order to accumulate enough statistics and thus reduce the uncertainty [36] of the autocorrelation function.

Representative curves are shown in Fig. 3(a), while results presented in Fig. 3(c) are obtained with additional averages obtained over 4 realizations. As demonstrated in Fig. 3(a), the angular autocorrelation function decreases rapidly with temperature and its trend is captured with fits

to a stretched exponential $\phi_{\mu-O}(\tau) = \exp[-(\lambda t)^{\beta}]$ which can reproduce the long time tail (for $t \to 0$, $\mu - O$ vibrations induce fast oscillations [67]). The values of λ and β are shown in Fig. 3(c) as a function of the inverse temperature. The muon mean square displacement MSD_μ is instead obtained from *ab initio* MD and is estimated as

$$\mathrm{MSD}_\mu(\tau) = \frac{1}{N_s - n_\tau} \sum_{j=1}^{N_s - n_\tau} |\mathbf{r}_\mu(t_j + \tau) - \mathbf{r}_\mu(t_j)|^2, \quad (2)$$

and the diffusion coefficient, defined by $D_\mu = \lim_{\tau\to\infty} \mathrm{MSD}_\mu(\tau)/(6\tau)$, is obtained from the MSD as the slope of the linear fits in the region highlighted in Fig. 3(b), obtained following Ref. [37], to ensure both linearity of the MSD at large τ [38] and exclusion of ballistic regime at small τ. Both λ and D_μ follow an activated behavior,

$$D_\mu(T) = D_0 e^{-E_A^D/k_B T}, \qquad \lambda(T) = \lambda_0 e^{-E_A^\phi/k_B T}, \quad (3)$$

as shown in Fig. 3(c). The activation energy obtained for the two processes is $E_A^\phi \sim 44(1)$ meV and $E_A^D \sim 0.23(16)$ eV and the infinite-temperature limits are $\lambda_0 = 0.01(1)$ fs^{-1} and $D_0 = 0.01(3)$ Å^2 fs^{-1}. The results for the former process can be roughly compared with the experimental estimates for the activation energy $E_A^{\mathrm{exp}} = 61$ meV and preexponential time $1/\tau_0^{\mathrm{exp}} = 0.169$ fs^{-1} of an activated hopping process [15,88]. Most importantly, the MD simulations show the presence of two diffusion mechanisms, one localized around oxygen atoms leading to the effective new site resulting from the motion average and experimentally observed above the magnetic transition and a second, conventional, diffusion process among oxygen atoms that justifies the second transition observed at high temperatures. We stress that the quantitative predictions should be taken with a grain of salt, since the quantum contributions to the muon motion are expected to be far from negligible in the temperature interval of rotational diffusion.

In conclusion, we have clarified the interpretation of the μSR signal of MnO—a puzzle that remained unsolved for over 40 years. The solution is naturally obtained from the accurate description of the magnetostriction effect that plays a fundamental role not only in the structural phase transition but also in the stabilization of different interstitial sites in the two phases of MnO. This leads to the observation of a single precession frequency below T_N and explains the unusual behaviors observed at higher temperatures. Indeed the particular network of muon sites stabilized in the cubic phase gives rise to two diffusion regimes, qualitatively captured by our MD simulations, that explain the low-temperature time dependence of the Knight shift and the second diffusion process observed experimentally above 500 K.

Our results highlight the fact that relatively small energy differences can play a fundamental role in the determination of the muon-sample interaction. This conclusion is applicable to the magnetic state of other transition-metal oxides whose μSR interpretation is still lacking [89,90] and provides an important ingredient to be considered in the analysis of experimental results of magnetic oxides that have recently attracted scientific attention owing to muon-induced effects [91,92].

P. B., I. J. O., and R. D. R. acknowledge financial support from PNRR MUR Project No. ECS_00000033_ECOSISTER. I. T., L. M., G. P., and N. M. acknowledge financial support from NCCR MARVEL, a National Centre of Competence in Research, funded by the Swiss National Science Foundation (Grant No. 205602). S. J. B. was funded by UK Research and Innovation (UKRI) under the UK government's Horizon Europe funding guarantee (Grant No. EP/X025861/1). Computer time was provided by the Swiss National Supercomputing Centre (CSCS) under Projects No. s1073 and No. s1192 and by the STFC Scientific Computing Department's SCARF cluster. The authors acknowledge Andrew Goodwin and Matthias Gutmann for sending their sample, sharing experimental detail, and for useful discussions, and Giuliana Materzanini for useful discussion on the MD analysis. The μSR experiments were carried out at the Swiss Muon Source (SμS), Paul Scherrer Insitute, Villigen.

*pietro.bonfa@unipr.it
†Present address: Deutsches Elektronen-Synchrotron DESY, 22607 Hamburg, Germany.

[1] *Muon Spectroscopy—An Introduction*, edited by S. J. Blundell, R. D. Renzi, T. Lancaster, and F. L. Pratt (Oxford University Press, Oxford, 2022).
[2] W. L. Roth, Phys. Rev. **110**, 1333 (1958).
[3] H. Shaked, J. Faber, and R. L. Hitterman, Phys. Rev. B **38**, 11901 (1988).
[4] A. K. Cheetham and D. A. O. Hope, Phys. Rev. B **27**, 6964 (1983).
[5] A. L. Goodwin, M. G. Tucker, M. T. Dove, and D. A. Keen, Phys. Rev. Lett. **96**, 047209 (2006).
[6] C. P. Gazzara and R. M. Middleton, Adv. X-Ray Anal. **9**, 152 (1965).
[7] G. Srinivasan and M. S. Seehra, Phys. Rev. B **28**, 6542 (1983).
[8] Y. Yamamoto and T. Nagamiya, J. Phys. Soc. Jpn. **32**, 1248 (1972).
[9] I. A. Blech and B. L. Averbach, Phys. Rev. **142**, 287 (1966).
[10] E. Uchida, H. Kondoh, Y. Nakazumi, and T. Nagamiya, J. Phys. Soc. Jpn. **15**, 466 (1960).
[11] B. Morosin, Phys. Rev. B **1**, 236 (1970).
[12] A. M. Balagurov, I. A. Bobrikov, S. V. Sumnikov, V. Y. Yushankhai, and N. Mironova-Ulmane, JETP Lett. **104**, 88 (2016).
[13] Y. J. Uemura, N. Nishida, J. Imazato, R. S. Hayano, M. Takigawa, and T. Yamazaki, Hyperfine Interact. **8**, 771 (1981).

[14] Y. J. Uemura, T. Yamazaki, Y. Kitaoka, M. Takigawa, and H. Yasuoka, Hyperfine Interact. **17**, 339 (1984).
[15] Y. J. Uemura, R. S. Hayano, J. Imazato, N. Nishida, K. Nagamine, T. Yamazaki, and H. Yasuoka, Hyperfine Interact. **6**, 127 (1979).
[16] Y. J. Uemura, J. Imazato, N. Nishida, R. S. Hayano, M. Takigawa, and T. Yamazaki, Hyperfine Interact. **8**, 725 (1981).
[17] K. Ishida, T. Matsuzaki, K. Nishiyama, and K. Nagamine, Hyperfine Interact. **19**, 927 (1984).
[18] U. Aschauer, N. Vonrüti, and N. A. Spaldin, Phys. Rev. B **92**, 054103 (2015).
[19] A. J. Logsdail, C. A. Downing, T. W. Keal, P. Sherwood, A. A. Sokol, and C. R. A. Catlow, J. Phys. Chem. C **123**, 8133 (2019).
[20] R. S. Hayano, Y. J. Uemura, J. Imazato, N. Nishida, K. Nagamine, T. Yamazaki, and H. Yasuoka, Phys. Rev. Lett. **41**, 421 (1978).
[21] E. Lidström and O. Hartmann, J. Phys. Condens. Matter **12**, 4969 (2000).
[22] B. Hermsmeier, J. Osterwalder, D. J. Friedman, and C. S. Fadley, Phys. Rev. Lett. **62**, 478 (1989).
[23] B. Hermsmeier, J. Osterwalder, D. J. Friedman, B. Sinkovic, T. Tran, and C. S. Fadley, Phys. Rev. B **42**, 11895 (1990).
[24] X. Sun, E. Feng, Y. Su, K. Nemkovski, O. Petracic, and T. Brückel, J. Phys. Conf. Ser. **862**, 012027 (2017).
[25] See Supplemental Material at http://link.aps.org/supplemental/10.1103/PhysRevLett.132.046701 for the details of the experimental setup, the computational methods, the details of the simulations, and the analysis of experimental and theoretical data, which includes Refs. [3,4,11,16,26–66].
[26] P. Hohenberg and W. Kohn, Phys. Rev. **136**, B864 (1964).
[27] W. Kohn and L. Sham, Phys. Rev. **140**, A1133 (1965).
[28] S. L. Dudarev, G. A. Botton, S. Y. Savrasov, C. J. Humphreys, and A. P. Sutton, Phys. Rev. B **57**, 1505 (1998).
[29] V. L. Campo Jr. and M. Cococcioni, J. Phys. Condens. Matter **22**, 055602 (2010).
[30] J. P. Perdew, A. Ruzsinszky, G. I. Csonka, O. A. Vydrov, G. E. Scuseria, L. A. Constantin, X. Zhou, and K. Burke, Phys. Rev. Lett. **100**, 136406 (2008).
[31] I. Timrov, N. Marzari, and M. Cococcioni, Phys. Rev. B **98**, 085127 (2018).
[32] I. Timrov, N. Marzari, and M. Cococcioni, Phys. Rev. B **103**, 045141 (2021).
[33] J. P. Perdew and A. Zunger, Phys. Rev. B **23**, 5048 (1981).
[34] I. J. Onuorah, P. Bonfà, and R. De Renzi, Phys. Rev. B **97**, 174414 (2018).
[35] I. J. Onuorah, P. Bonfà, R. De Renzi, L. Monacelli, F. Mauri, M. Calandra, and I. Errea, Phys. Rev. Mater. **3**, 073804 (2019).
[36] I. Bitsanis, M. Tirrell, and H. T. Davis, Phys. Rev. A **36**, 958 (1987).
[37] R. Zwanzig and N. K. Ailawadi, Phys. Rev. **182**, 280 (1969).
[38] X. He, Y. Zhu, A. Epstein, and Y. Mo, npj Comput. Mater. **4**, 18 (2018).
[39] A. García *et al.*, J. Chem. Phys. **152**, 204108 (2020).
[40] S. Baroni, S. de Gironcoli, A. Dal Corso, and P. Giannozzi, Rev. Mod. Phys. **73**, 515 (2001).
[41] J. W. Bennett, B. G. Hudson, I. K. Metz, D. Liang, S. Spurgeon, Q. Cui, and S. E. Mason, Comput. Mater. Sci. **170**, 109137 (2019).
[42] P. Bonfà and R. De Renzi, J. Phys. Soc. Jpn. **85**, 091014 (2016).
[43] S. Chmiela, V. Vassilev-Galindo, O. T. Unke, A. Kabylda, H. E. Sauceda, A. Tkatchenko, and K.-R. Müller, Sci. Adv. **9**, eadf0873 (2023).
[44] M. Cococcioni and S. de Gironcoli, Phys. Rev. B **71**, 035105 (2005).
[45] A. Dal Corso, Comput. Mater. Sci. **95**, 337 (2014).
[46] K. F. Garrity, J. W. Bennett, K. M. Rabe, and D. Vanderbilt, Comput. Mater. Sci. **81**, 446 (2014).
[47] P. Giannozzi, O. Baseggio, P. Bonfà, D. Brunato, R. Car, I. Carnimeo, C. Cavazzoni, S. De Gironcoli, P. Delugas, F. Ferrari Ruffino *et al.*, J. Chem. Phys. **152**, 154105 (2020).
[48] P. Giannozzi *et al.*, J. Phys. Condens. Matter **21**, 395502 (2009).
[49] P. Giannozzi *et al.*, J. Phys. Condens. Matter **29**, 465901 (2017).
[50] Davide Ceresoli, GIPAW code, https://github.com/dceresoli/qe-gipaw (accessed on 2023-05-12).
[51] T. Gorni, I. Timrov, and S. Baroni, Eur. Phys. J. B **91**, 249 (2018).
[52] E. Kucukbenli, M. Monni, B. Adetunji, X. Ge, G. Adebayo, N. Marzari, S. de Gironcoli, and A. Dal Corso, arXiv:1404.3015.
[53] H. Kulik and N. Marzari, J. Chem. Phys. **134**, 094103 (2011).
[54] P.-O. Löwdin, J. Chem. Phys. **18**, 365 (1950).
[55] The SSSP library of the Materials Cloud, https://www.materialscloud.org/discover/sssp/table/precision.
[56] P. Bonfà, I. John Onuorah, F. Lang, I. Timrov, L. Monacelli, C. Wang, X. Sun, O. Petracic, G. Pizzi, N. Marzari, S. J. Blundell, and R. De Renzi, Magnetostriction-driven muon localisation in an antiferromagnetic oxide, Materials Cloud Archive 2023.82, 10.24435/materialscloud:8s-qh.
[57] I. Mayer, Int. J. Quantum Chem. **90**, 63 (2002).
[58] A. Baldereschi, Phys. Rev. B **7**, 5212 (1973).
[59] G. Prandini, A. Marrazzo, I. E. Castelli, N. Mounet, and N. Marzari, npj Comput. Mater. **4**, 1 (2018).
[60] F. Pratt, Physica (Amsterdam) **289–290B**, 710 (2000).
[61] I. Timrov, F. Aquilante, L. Binci, M. Cococcioni, and N. Marzari, Phys. Rev. B **102**, 235159 (2020).
[62] I. Timrov, N. Marzari, and M. Cococcioni, Comput. Phys. Commun. **279**, 108455 (2022).
[63] Y.-C. Wang, Z.-H. Chen, and H. Jiang, J. Chem. Phys. **144**, 144106 (2016).
[64] C. Tablero, J. Phys. Condens. Matter **20**, 325205 (2008).
[65] B. Amadon, F. Jollet, and M. Torrent, Phys. Rev. B **77**, 155104 (2008).
[66] K. Nawa, T. Akiyama, T. Ito, K. Nakamura, T. Oguchi, and M. Weinert, Phys. Rev. B **97**, 035117 (2018).
[67] A. Mattoni, A. Filippetti, M. I. Saba, and P. Delugas, J. Phys. Chem. C **119**, 17421 (2015).
[68] V. I. Anisimov, J. Zaanen, and O. K. Andersen, Phys. Rev. B **44**, 943 (1991).
[69] DFT simulations do not identify the small monoclinic distortion for MnO; see, for example, Ref. [70].
[70] A. Schrön, C. Rödl, and F. Bechstedt, Phys. Rev. B **86**, 115134 (2012).
[71] E. M. L. Chung, D. M. Paul, G. Balakrishnan, M. R. Lees, A. Ivanov, and M. Yethiraj, Phys. Rev. B **68**, 140406(R) (2003).

[72] J. S. Lim, D. Saldana-Greco, and A. M. Rappe, Phys. Rev. B **94**, 165151 (2016).
[73] J. E. Pask, D. J. Singh, I. I. Mazin, C. S. Hellberg, and J. Kortus, Phys. Rev. B **64**, 024403 (2001).
[74] C. Franchini, V. Bayer, R. Podloucky, J. Paier, and G. Kresse, Phys. Rev. B **72**, 045132 (2005).
[75] A. Mellergård, R. L. McGreevy, A. Wannberg, and B. Trostell, J. Phys. Condens. Matter **10**, 9401 (1998).
[76] M. Bonfante, B. Hennion, F. Moussa, and G. Pepy, Solid State Commun. **10**, 553 (1972).
[77] C. H. Wang, S. N. Baker, M. D. Lumsden, S. E. Nagler, W. T. Heller, G. A. Baker, P. D. Deen, L. M. D. Cranswick, Y. Su, and A. D. Christianson, Phys. Rev. B **83**, 214418 (2011).
[78] B. Huddart, A. Hernández-Melián, T. Hicken, M. Gomilšek, Z. Hawkhead, S. Clark, F. Pratt, and T. Lancaster, Comput. Phys. Commun. **280**, 108488 (2022).
[79] We performed collinear DFT simulations; therefore the direction of $\mathbf{S}_e$ cannot be established. See Supplemental Material for more details on the approximations concerning the evaluation of the Fermi contact field [25].
[80] B. A. Frandsen and S. J. L. Billinge, Acta Crystallogr. Sect. A **71**, 325 (2015).
[81] S. Massidda, M. Posternak, A. Baldereschi, and R. Resta, Phys. Rev. Lett. **82**, 430 (1999).
[82] W. Jauch and M. Reehuis, Phys. Rev. B **67**, 184420 (2003).
[83] J.-P. Vidal, G. Vidal-Valat, K. Kurki-Suonio, and R. Kurki-Suonio, Crystallogr. Rep. (Transl. Kristallografiya) **47**, 347 (2002).
[84] In a spin-unpolarized simulation the energy difference vanishes.
[85] S. Lee, Y. Ishikawa, P. Miao, S. Torii, T. Ishigaki, and T. Kamiyama, Phys. Rev. B **93**, 064429 (2016).
[86] P. Kofstad, J. Phys. Chem. Solids **44**, 879 (1983).
[87] A. Z. Hed and D. S. Tannhauser, J. Chem. Phys. **47**, 2090 (2004).
[88] The experimental estimate includes a correction due to the electronic correlation time; see cited reference for details.
[89] K. Nishiyama, W. Higemoto, K. Shimomura, A. Koda, G. Maruta, S. W. Nishiyama, and X. G. Zheng, Hyperfine Interact. **136**, 289 (2001).
[90] K. Nishiyama, S. Ohira, W. Dawson, and W. Higemoto, Hyperfine Interact. **104**, 349 (1997).
[91] M. H. Dehn, J. K. Shenton, D. J. Arseneau, W. A. MacFarlane, G. D. Morris, A. Maigné, N. A. Spaldin, and R. F. Kiefl, Phys. Rev. Lett. **126**, 037202 (2021).
[92] M. H. Dehn, J. K. Shenton, S. Holenstein, Q. N. Meier, D. J. Arseneau, D. L. Cortie, B. Hitti, A. C. Y. Fang, W. A. MacFarlane, R. M. L. McFadden, G. D. Morris, Z. Salman, H. Luetkens, N. A. Spaldin, M. Fechner, and R. F. Kiefl, Phys. Rev. X **10**, 011036 (2020).